

Research Article

Performance Evaluation of FSO Communications under Sand-Dust Conditions

Minghua Cao ¹, Huiqin Wang ¹, Yu Yao ² and Shanglin Hou ³

¹School of Computer and Communication, Lanzhou University of Technology, Lanzhou 730050, China

²Lanzhou Electric Power Supply Company, State Grid Corporation of China, Lanzhou 730050, China

³School of Science, Lanzhou University of Technology, Lanzhou 730050, China

Correspondence should be addressed to Minghua Cao; caomh315@163.com

Received 27 March 2019; Accepted 5 October 2019; Published 31 October 2019

Academic Editor: Lorenzo Luini

Copyright © 2019 Minghua Cao et al. This is an open access article distributed under the Creative Commons Attribution License, which permits unrestricted use, distribution, and reproduction in any medium, provided the original work is properly cited.

Sand-dust weather conditions are considered the primary challenge to free-space optical (FSO) communications. It may cause severe attenuation that is malignant to FSO link performance. This study investigates the impact of sand-dust particles on a laser signal using the radiation propagation method and the small-angle approximation method. Numerical simulation shows that in sand-dust weather conditions, the multiple scattering effect is dominant and results in signal pulse delay and pulse broadening. Furthermore, the signal attenuation follows a negative exponential distribution to the laser wavelength. Superior performance can be achieved by employing a longer wavelength laser to reduce pulse delay and mutual interference.

1. Introduction

Free-space optical communication (FSO) is considered one of the most promising alternatives in metropolitan and local area networks as a viable solution to the access network last mile problem, in which a compromise between the available data rates and the cost is desirable [1, 2]. However, the performance of an FSO system is dependent on atmospheric conditions, particularly in the presence of aerosols (e.g., fog, smoke, sand-dust, and water vapour) which result in scattering and absorption effects [3–5]. Combined with aerosols, sand-dust particles may cause serious transmission interruption. Therefore, we focus on FSO link performance under sand-dust weather conditions to accurately predict the impact of sand-dust particles on FSO transmission.

Early researches on laser scattering primarily utilized Lambert–Beer’s law to analyse the single scattering of spherical particles [6–8]. However, it is insufficient to analyse only the single scattering scenario because the corresponding optical thickness increases with increasing transmission distance and atmospheric visibility. To resolve this issue, Islam proposed a simple model for the calculation

of signal attenuation induced by sand-dust particles [9]. Wang investigated the influence of atmospheric visibility on pulse delay and pulse broadening through Mie theory and Monte Carlo method [10]. The spherical shape of the sand-dust particle is assumed in all these researches. However, the geometries of sand-dust particles cannot be classified as spheres, ellipsoids, cubes, or otherwise. Thus, the results may not be sufficiently accurate to describe the practical situation in FSO links.

On the problem of nonspherical particle scattering, Mackowski proposed a computational method to calculate the T-matrix of arbitrary-shaped particles by introducing moment solution to the discrete dipole approximation interaction equations [11]. Wang employed the finite element method to evaluate three types of boundary conditions and modelled the light propagation process in turbid media [12]. These researches provide novel perspectives to the problem of laser signal transmission under sand-dust weather conditions. Drawing inspiration from these researches, the radiation propagation method and the small-angle approximation method were utilized in this study to macroscopically analyse the characteristics of laser transmission in a sand-dust channel.

2. Theoretical Analysis

2.1. Laser Intensity. When a laser transmits in the scattering medium, its intensity can be expressed as

$$\frac{dL(e, e_s)}{ds} = -\rho C_e L(e, e_s) + \rho C_e \int_{4\pi} p(e_s, e'_s) L(e, e'_s) d\alpha' + \varepsilon(e, e_s), \quad (1)$$

where $L(e, e_s)$ is the light intensity, e is the particle position, e_s is the incident laser direction, e'_s is the scattering light direction from other particles, ρ is the particle density, and $p(e_s, e'_s)$ is the scattering phase function. $C_e = C_a + C_s$ is the extinction coefficient, where C_a and C_s represent the absorption coefficient and the scattering coefficient, respectively. Assume α as the solid angle of the scattering light, α' as the solid angle of the e'_s direction, and $\varepsilon(e, e_s)$ as the radiation power of a unit volume along the e_s direction. Consequently, equation (1) can be illustrated by Figure 1.

It is evident from the plot that the received signal consists of three main parts: (1) the attenuated signal in the e_s direction which went through the particle scattering and absorption effects; (2) the signal from other directions, e.g., e'_s , which are superimposed on the e_s direction; and (3) the signal emitted by the internal radiation source in the e_s direction.

Assume the medium is completely absorptive and the photons follow the elastic scattering mode, and equation (1) can be simplified as

$$\frac{dL(e, e_s)}{d\tau} = -L(e, e_s) + \int_{4\pi} p(e_s, e'_s) L(e, e'_s) d\alpha', \quad (2)$$

where $\tau = \int \rho C_e ds$ denotes the optical thickness. $p(e_s, e'_s)$ can be unfolded by the Legendre function as

$$p(\theta, \varphi; \theta', \varphi') = \sum_{j=0}^{\infty} \sum_{i=j}^{\infty} d_i^j P_i^j(\cos \theta) P_i^j(\cos \theta') \cos[j(\varphi - \varphi')], \quad (3)$$

where θ and φ denote the zenith angle and azimuth angle of the incident light, respectively; θ' and φ' denote the zenith angle and azimuth angle of the emitting light, respectively; $P_i^j(\cos \theta)$ denotes the Legendre function; and d_i^j denotes the Legendre constant.

In contrast, equation (2) can be expressed in Cartesian coordinates as

$$\cos \theta \frac{dL(z, \theta)}{d\theta} = -C_e L(z, \theta) + \frac{C_s}{2} \int_0^\pi p(\theta, \theta') L(z, \theta') \sin \theta' d\theta'. \quad (4)$$

When it is assumed that $\mu = \cos \theta$, $\mu' = \cos \theta'$, and $j \neq 0$, $\int_0^{2\pi} \cos[j(\varphi - \varphi')] d\varphi' = 0$. Furthermore, when the scattering phase function is assumed as $p(\mu, \mu') = \sum_{i=0}^{\infty} d_i P_i(\mu) P_i(\mu')$ and the scattering albedo as $\omega = C_s/C_e$, equation (4) can be simplified as

$$\mu \frac{dL(\tau, \mu)}{d\tau} = -L(\tau, \mu) + \frac{\omega}{2} \int_{-1}^1 p(\mu, \mu') L(\tau, \mu') d\mu'. \quad (5)$$

However, the laser beam will gradually be deviated away from the optical axis due to the sand-dust particles'

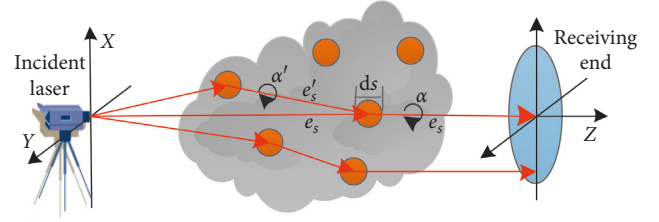


FIGURE 1: Schematic geometry of radiative transmission.

multiple scattering effect. Therefore, the light intensity can be expanded by the sum of the scattered lights [13]:

$$L(\tau, \mu) = \sum_{m=0}^{\infty} L_m(\tau, \mu). \quad (6)$$

If the scattered laser from other directions can be neglected, the light intensity can be derived by a recursive relation as

$$L_m(\tau, \mu) = \int_0^\tau J_m(\tau', \mu) \exp\left(-\frac{\tau - \tau'}{\mu}\right) \frac{d\tau'}{\mu}, \quad (7)$$

where

$$J_m(\tau, \mu) = \frac{\omega}{2} \int_{-1}^1 p(\mu, \mu') L_{m-1}(\tau, \mu') d\mu', \quad (8)$$

where m is the scattering number which satisfies $m \geq 1$.

Considering that the laser wavelength is much smaller than the average radius of the sand-dust particles, the sand-dust particles show a significant forward scattering selectivity in the light. Consequently, the laser power is concentrated mainly in a very small range along the propagation direction.

Substituting equations (7) and (8) into equation (6), it can then be expressed in the form of $L_m(\tau, \mu) = A_m(\tau, \mu_0) B_m(\mu, \mu_0)$, where μ_0 denotes the initial value of $\cos \theta$ before scattering:

$$B_m(\mu, \mu_0) = \frac{\omega}{2} \int_{-1}^1 p(\mu, \mu') B_{m-1}(\mu', \mu_0) d\mu', \quad (9)$$

$$A_m(\tau, \mu_0) = \int_0^\tau A_{m-1}(\tau', \mu_0) \exp\left(-\frac{\tau - \tau'}{\mu}\right) \frac{d\tau'}{\mu}. \quad (10)$$

According to the orthogonality of the Legendre polynomials, $\int_{-1}^1 P_i(\mu) P_j(\mu) d\mu = (\delta_{i,j} / (i + 1/2))$, where $\delta_{i,j} = \begin{cases} 1, & i = j, \\ 0, & i \neq j, \end{cases}$. Therefore, equation (9) can be rewritten as

$$B_m(\mu, \mu_0) = \omega^m \sum_{i=0}^{\infty} \left(i + \frac{1}{2}\right) d_i^m P_i(\mu) P_i(\mu_0). \quad (11)$$

According to small-angle approximation (where $\mu = \mu_0$ and $\mu' \approx \mu$), equation (10) can be rewritten as

$$A_1(\tau, \mu_0) = \int_0^\tau A_0(\tau', \mu_0) \exp\left(-\frac{\tau - \tau'}{\mu}\right) \frac{d\tau'}{\mu} = E_0 \exp\left(-\frac{\tau}{\mu}\right) \cdot \int_0^\tau \exp\left(\frac{\mu_0 - \mu}{\mu_0 \mu} \tau'\right) \frac{d\tau'}{\mu} \approx E_0 \exp\left(-\frac{\tau}{\mu_0}\right) \frac{\tau}{\mu_0}, \quad (12)$$

$$A_m(\tau, \mu_0) = \int_0^\tau A_{m-1}(\tau', \mu_0) \exp\left(-\frac{\tau - \tau'}{\mu}\right) \frac{d\tau'}{\mu} \approx E_0 \frac{1}{m!} \cdot \left(\frac{\tau}{\mu_0}\right)^m \exp\left(-\frac{\tau}{\mu_0}\right), \quad (13)$$

where E_0 denotes the initial laser intensity.

Substituting equations (11) and (13) into equation (6), the light intensity of multiple scattering can be expressed as

$$L(\tau, \mu) = \sum_{m=0}^{\infty} A_m(\tau, \mu_0) B_m(\mu, \mu_0) \approx \sum_{m=0}^{\infty} E_0 B_m(\mu, \mu_0) \cdot \frac{(\tau/\mu_0)^m}{m!} \exp\left(-\frac{\tau}{\mu_0}\right). \quad (14)$$

In contrast, the laser intensity without scattering can be written as

$$L_0(\tau, \mu) = E_0 \exp\left(-\frac{\tau}{\mu_0}\right) \delta(\mu - \mu_0), \quad (15)$$

where δ is the Dirac function.

2.2. Laser Pulse Characteristics. The scattering of sand-dust particles leads to light intensity attenuation. It also results in laser pulse delay and pulse broadening. Suppose a laser beam is transmitting along the z -axis, and a sand-dust particle lies at the original point O . The laser propagation direction will be deflected to point P due to the scattering effect, as described in Figure 2. The average photon path length per unit time (denoted as dR/dt) can be expressed as

$$\frac{dR}{dt} = \left[\left(\frac{dx}{dt}\right)^2 + \left(\frac{dy}{dt}\right)^2 + \left(\frac{dz}{dt}\right)^2 \right]^{1/2}. \quad (16)$$

According to the classical electron scattering theory [14], the scattering projection angle α can be written as

$$\alpha = (\omega\tau\theta_0^2)^{1/2}, \quad (17)$$

where θ is the scattering angle and $\theta_0^2 = \int_0^\pi \theta^2 p(\theta) d\theta$. $p(\theta)$ is the scattering phase function, which describes the laser power spatial distribution after scattering.

A revised two-term Henyey-Greenstein (TTHG) scattering phase function is proposed in [15]. The authors use two asymmetric factors to consider both forward scattering and backward scattering. Consequently, the $p(\theta)$ function can be expressed as

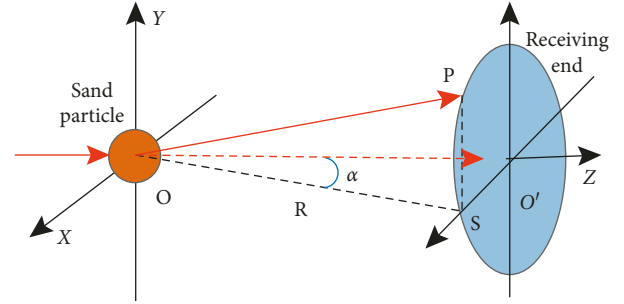


FIGURE 2: Geometrical schematic of laser scattering.

$$p(\mu; \lambda, g_1, g_2) = \lambda p(\mu; g_1) + (1 - \lambda) p(\mu; g_2)$$

$$= \lambda \frac{1 - g_1^2}{(1 - 2\mu g_1 + g_1^2)^{3/2}} + (1 - \lambda) \frac{1 - g_2^2}{(1 - 2\mu g_2 + g_2^2)^{3/2}}, \quad (18)$$

where g_1 and g_2 denote the asymmetric factor parameters, and the asymmetric factor $g = \lambda g_1 + (1 - \lambda) g_2$, $0 \leq \lambda \leq 1$, $g_1 \cdot g_2 \leq 0$.

According to Koschmieder's law [16], the relationship between atmospheric visibility (V) and the extinction coefficient (C_e) can be written as

$$C_e = \frac{3.91}{V} \left(\frac{\lambda}{0.55}\right)^{-q}, \quad (19)$$

where λ is the laser wavelength, and q is a parameter related to atmospheric visibility, which is described by the following equations:

$$q = \begin{cases} 0.585V^{1/3}, & V < 6 \text{ km}, \\ 1.3, & 6 \text{ km} \leq V < 50 \text{ km}, \\ 1.6, & V \geq 50 \text{ km}. \end{cases} \quad (20)$$

According to the particle forward scattering selectivity and the small-angle approximation theory, $\tan \theta \approx \theta$. Therefore, the x -direction component can be expressed as

$$x = z \cdot \tan(\omega\tau\theta_0^2)^{1/2} \approx z \cdot (\omega\tau\theta_0^2)^{1/2}, \quad (21)$$

$$\frac{dx}{dz} = \frac{3}{2} (\omega\tau\theta_0^2)^{1/2}. \quad (22)$$

Since the y -direction component of the XOZ plane is 0, the average laser scattering path length is

$$\frac{dR}{dz} = \left[\frac{9}{4} (\omega\tau\theta_0^2) + 1 \right]^{1/2}. \quad (23)$$

Integral to both sides of equation (23), the photon scattering path length R is

$$R = \frac{0.3z}{\omega\tau\theta_0^2} \left[\left(\frac{9}{4} \omega\tau\theta_0^2 + 1 \right)^{3/2} - 1 \right]. \quad (24)$$

As a result, the pulse delay Δt can be expressed as

$$\Delta t = \frac{R-z}{c} = \frac{z \cdot n}{c} \cdot \left\{ \frac{0.3}{\omega \tau \theta_0^2} \left[\left(\frac{9}{4} \omega \tau \theta_0^2 + 1 \right)^{3/2} - 1 \right] - 1 \right\}, \quad (25)$$

where n denotes the complex refractive index of sand-dust particles, and $c = 3 \times 10^8$ m/s is the speed of light in a vacuum. It is evident from equation (25) that the laser pulse delay in sand-dust conditions is related to the parameters of transmission distance, optical thickness, scattering angle, scattering coefficient, and attenuation coefficient. Furthermore, the laser pulse delay is in direct proportion to the transmission distance and the sand-dust complex refractive index.

However, the pulse delay is in nanosecond order of magnitude, and the scattering process can be considered as a laser pulse throughout a linear time-invariant system. Consequently, the signal at the receiver end can be expressed as

$$y(t) = f(t) * P_s(t), \quad (26)$$

where $f(t)$ denotes the laser pulse, which follows the Gaussian distribution and can be expressed as

$$f(t) = \exp\left(-\frac{\ln(16)}{T_0^2} t^2\right), \quad (27)$$

where T_0 is the pulse width. $P_s(t)$ denotes the normalized pulse power, which can be expressed as [17]

$$P_s(t) = E_R \frac{t}{\Delta t^2} \exp\left(-\frac{t}{\Delta t}\right), \quad t \geq 0, \quad (28)$$

where E_R is the unit pulse power of the received laser signal.

Substituting equations (27) and (28) into equation (26), the received signal is

$$y(t) = f(t) * P_s(t) = \int_0^\infty E_R \frac{\xi}{\Delta t^2} \exp\left(-\frac{\xi}{\Delta t} - \frac{\ln(16)}{T_0^2} (t-\xi)^2\right) d\xi. \quad (29)$$

The received signal is primarily related to the parameters of normalized pulse power, pulse delay, and pulse width.

Defining t_m as a 3 dB pulse time extension width of $P_s(t)$,

$$\int_0^{2t_m} \frac{1}{E_R} P_s(t) dt = 95.6\%. \quad (30)$$

This indicates that 95.6% of the pulse power is concentrated in $2t_m$. Therefore, the amount of pulse broadening can be written as

$$t_m = 2.45\Delta t = \frac{z \cdot n}{c} \cdot \left\{ \frac{0.735}{\omega \tau \theta_0^2} \left[\left(\frac{9}{4} \omega \tau \theta_0^2 + 1 \right)^{3/2} - 1 \right] - 2.45 \right\}. \quad (31)$$

It is evident from equation (31) that the amount of laser pulse broadening is affected primarily by the parameter of time delay and is related to the parameters of transmission distance, sand-dust particle refractive index, scattering albedo, optical thickness, and scattering angle.

2.3. Light Attenuation. Sand-dust concentration describes the quantity of sand-dust particles within a unit volume, which directly reflects the severity of the sand-dust weather condition [18]. The distribution of the sand-dust concentration with a certain particle size can be expressed as [19]

$$W = \frac{\pi}{6} G \rho 10^{-9} \int_0^\infty r^3 p(r) dr = 0.001388 \rho \int_0^\infty r^3 p(r) dr, \quad (32)$$

where $G = 2.65 \times 10^6$ g/m³ denotes the sand-dust proportion; r denotes the radius of sand-dust particles; and $p(r)$ denotes the sand-dust particle radius distribution, which normally follows the log-normal distribution [20].

Therefore, the probability density distribution function of the sand-dust particle radius can be written as

$$N(r) = \frac{p(r)}{\rho}. \quad (33)$$

According to Koschmieder's law, the relationship between atmospheric visibility V and the attenuation coefficient C_e is

$$V = \frac{15}{C_e}, \quad (34)$$

$$C_e = 8.686 \times 10^{-3} \pi \rho \int_0^\infty r^2 N(r) dr. \quad (35)$$

In terms of atmospheric visibility [21], ρ can be expressed as

$$\rho = \frac{15}{8.686 \times 10^3 \pi V \int_0^\infty r^2 N(r) dr}. \quad (36)$$

Additionally, the relationship between atmospheric visibility and antenna transmission height can be demonstrated as [22]

$$V = V_0 \times \exp(bh), \quad (37)$$

where h is the vertical height, $b = 1.25$, and V_0 denotes horizontal visibility near the ground.

Substituting equations (36) and (37) into equation (32), the distribution of sand-dust particle concentration can be expressed as

$$W = \frac{5.085 \times 10^{-8} \int_0^\infty r^3 p(r) dr}{V_0 \exp(1.25h) \int_0^\infty r^2 N(r) dr}. \quad (38)$$

However, sand-dust particles are randomly distributed in the air and can be considered as composite media composed of dry sand-dust particles and moisture. Its complex permittivity is determined by the dielectric constant of sand and moisture and varies with frequency. According to the Maxwell-Garnett equations, the complex permittivity of sand-dust particles takes the form [23]

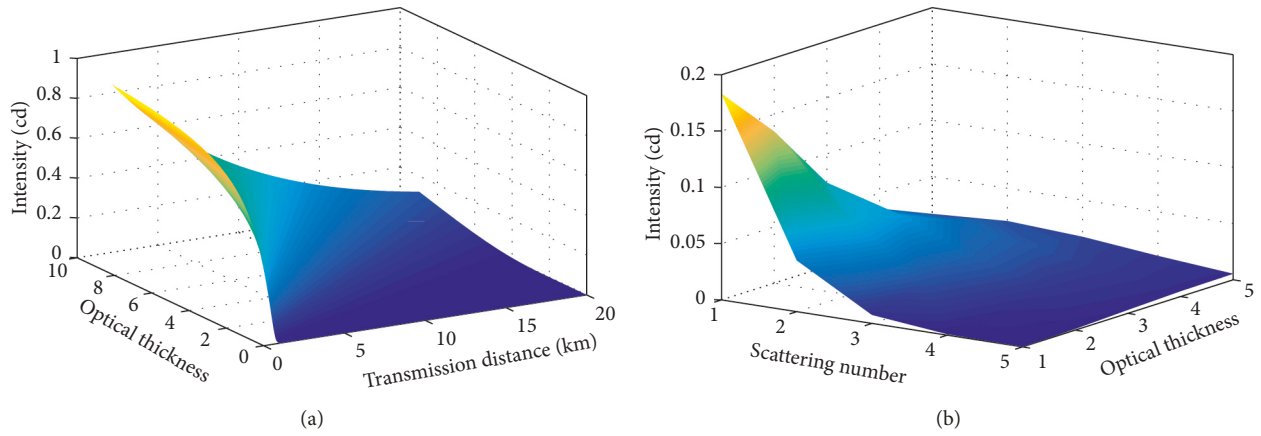


FIGURE 3: Laser intensity under (a) single scattering scenario and (b) multiple scattering scenarios.

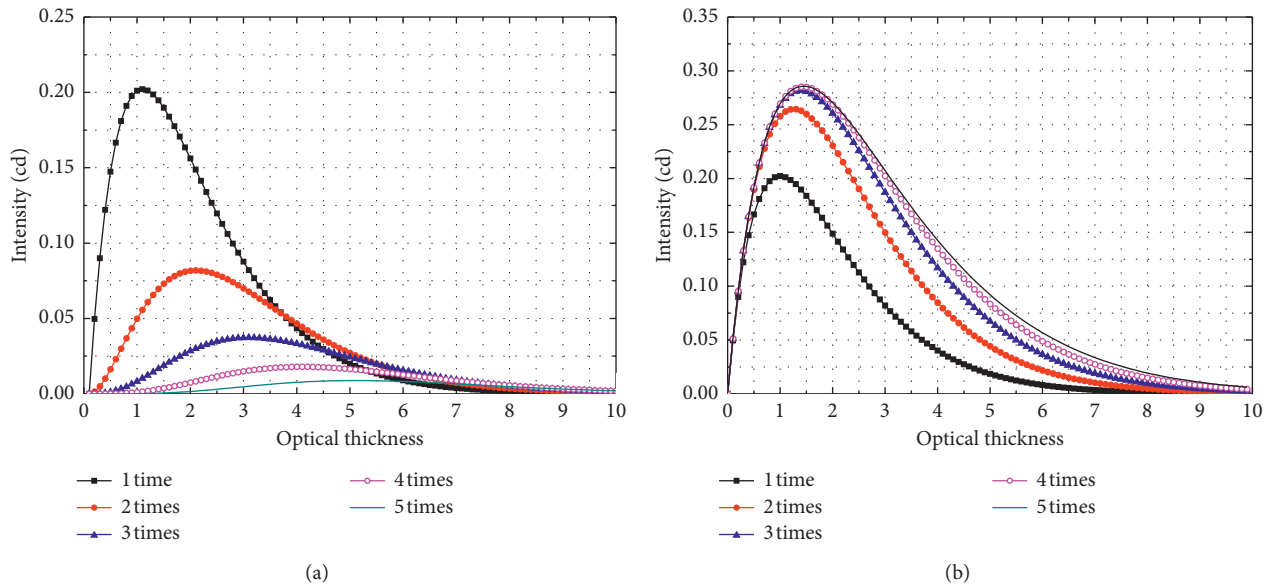


FIGURE 4: Laser intensity versus the optical thickness for (a) laser intensity of different scattering times and (b) total received laser intensity of different scattering times.

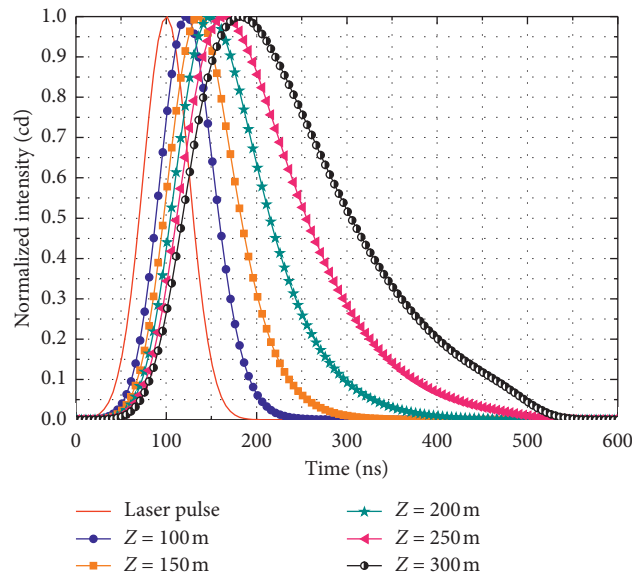


FIGURE 5: The normalized laser pulse waveform at different transmission distances.

TABLE 1: Received pulse width at different transmission distances.

Transmission distances (m)	Received pulse width (ns)
Initial pulse width	100
100	121
150	136
200	149
250	166
300	182

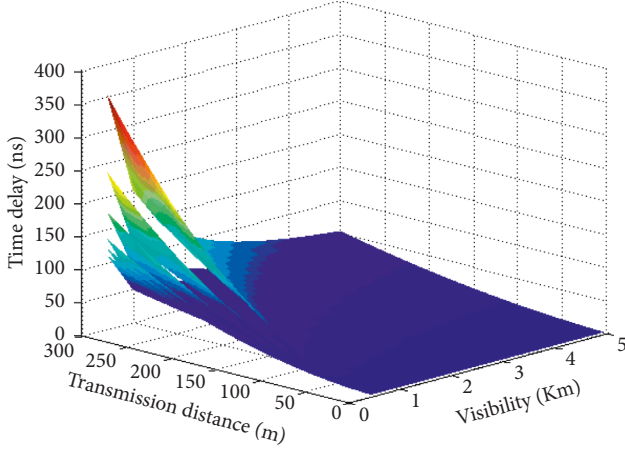


FIGURE 6: The pulse time delay versus the transmission distance and atmospheric visibility under different laser wavelengths.

$$\epsilon_e = \epsilon_r + i\epsilon_i = \epsilon_s \left[1 + \frac{3P((\epsilon_w - \epsilon_s)/(\epsilon_w + 2\epsilon_s))}{1 - P((\epsilon_w - \epsilon_s)/(\epsilon_w + 2\epsilon_s))} \right], \quad (39)$$

where ϵ_r and ϵ_i are the real and imaginary parts of ϵ_e , P denotes the volume fraction occupied by sand-dust particles in a unit volume, and ϵ_s and ϵ_w denote the complex permittivity of dry sand-dust particles and the relative dielectric constant of moisture, respectively. According to Wang et al. [24], the real parts ϵ'_s and imaginary parts ϵ''_s of ϵ_s are

$$\left\{ \begin{array}{l} \epsilon'_s = 3, \\ \epsilon''_s = \begin{cases} \frac{1.8 \times 10^{(2\lg f - 2.8)}}{f}, & 0.8 \text{ GHz} \leq f < 80 \text{ GHz}, \\ \frac{18.256}{f}, & f \geq 80 \text{ GHz}. \end{cases} \end{array} \right. \quad (40)$$

According to the empirical formula proposed by Ellison [25], the real parts ϵ'_w and imaginary parts ϵ''_w of ϵ_w are

$$\left\{ \begin{array}{l} \epsilon'_w = \epsilon_{\infty} + \frac{(\epsilon_1 - \epsilon_{\infty}) [1 - (\lambda_s/\lambda)^{1-\alpha} \sin(\alpha\pi/2)]}{1 + 2(\lambda_s/\lambda)^{1-\alpha} \sin(\alpha\pi/2) + (\lambda_s/\lambda)^{2(1-\alpha)}}, \\ \epsilon''_w = \epsilon_{\infty} + \frac{(\epsilon_1 - \epsilon_{\infty}) (\lambda_s/\lambda)^{1-\alpha} \cos(\alpha\pi/2)}{1 + 2(\lambda_s/\lambda)^{1-\alpha} \sin(\alpha\pi/2) + (\lambda_s/\lambda)^{2(1-\alpha)}} + \frac{\sigma_w \lambda}{18.8496 \times 10^{10}}, \end{array} \right. \quad (41)$$

where $\sigma_w = 12.5664 \times 108 \text{ S} \cdot \text{m}^{-1}$; and α , λ_s , ϵ_1 , and ϵ_{∞} are four atmospheric temperature-dependent quantities.

Consequently, the light attenuation in sand-dust weather conditions can be written as [26]:

$$A = \frac{92.7 \cdot \epsilon_i}{(\epsilon_r + 2)^2 + \epsilon_i^2} \cdot \frac{W}{\lambda}, \quad (42)$$

where, ϵ_r and ϵ_i are the real and imaginary parts of ϵ_e and λ is the laser wavelength.

Substituting equations (39)–(41) into equation (42), the light attenuation in sand-dust weather conditions can be derived as

$$A = \frac{4.714 \times 10^{-6} \cdot \epsilon_i \int_0^{\infty} r^3 p(r) dr}{\lambda \cdot V_0 \cdot ((\epsilon_r + 2)^2 + \epsilon_i^2) \cdot \exp(1.25h) \int_0^{\infty} r^2 N(r) dr}. \quad (43)$$

3. Numerical Evaluation

Numerical simulations were carried out based on the preceding derivation. The simulation parameters were set as follows: the initial light intensity $E_0=1$, the signal pulse width $T_0=60 \text{ ns}$, the temperature $t=20^\circ\text{C}$, and $n=1.55-0.005i$, where the real part of n indicates the scattering capacity and the imaginary part of n indicates the absorption capacity.

3.1. Laser Intensity. According to Mie theory and equation (14), the laser intensity under single and multiple scattering scenarios are shown in Figures 3 and 4.

It is evident from Figure 3(a) that the laser intensity is directly proportional to the optical thickness and inversely proportional to the transmission distance in the single scattering scenario. Figure 3(b) shows that the laser intensity is inversely proportional to the scattering number and the optical thickness. The laser intensity follows exponential decay to the scattering number and the optical thickness.

Figure 4(a) illustrates the laser intensity versus the atmospheric optical thickness for different scattering number values. It can be observed that the maximum value is between 1 and 3. Furthermore, the laser intensity decreases rapidly with increasing scattering number values. This indicates that the multiple scattering will strongly attenuate the laser intensity in sand-dust weather conditions. In contrast, the laser intensity of multiple scattering is slightly larger than that of single scattering when the optical thickness is more than 5. This indicates that multiple scattering is dominant in the sand-dust channel when the optical thickness is high. The total received laser intensity versus the atmospheric optical thickness for different scattering number values is depicted in Figure 4(b). It is evident from the figure that the total received laser intensity increases with increasing scattering number values. The reason for this phenomenon is that the total received laser intensity is comprised of the single scattering light and the corresponding multiple scattering lights. Moreover, the total received laser intensity changes a little when the scattering number is more than

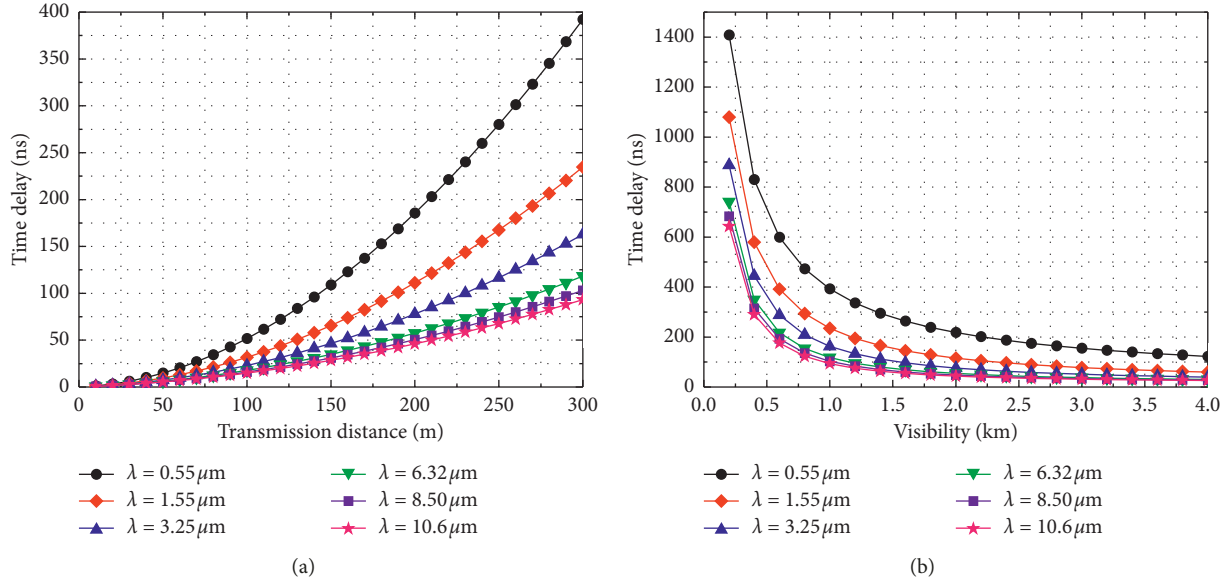


FIGURE 7: Pulse time delay of different laser wavelengths at (a) various transmission distances and (b) various atmospheric visibilities.

TABLE 2: Pulse time delay of different laser wavelengths.

Laser wavelength (μm)	Pulse time delay (ns)
10.60	93.2
8.50	103.1
6.32	118.3
3.25	162.8
1.55	234.6
0.55	392.1

three. Therefore, it can be inferred that the laser intensity of multiple scattering of more than three can be ignored.

3.2. Laser Pulse Characteristics. The received laser pulse waveform and the laser pulse characteristics under sand-dust weather conditions are shown in Figures 5–9 based on equations (15) and (29).

Figure 5 demonstrates the normalized laser pulse waveform at different transmission distances, where the scattering albedo is set as $\omega = 0.5$, and the scattering coefficient is set as $C_s = 7 \times 10^{-4}$. The figure indicates that pulse width will broaden with increasing transmission distance. Table 1 shows the extended received pulse width with the different transmission distances, where the initial pulse width is set as 100 ns.

Figure 6 illustrates the effect of transmission distance and atmospheric visibility on laser pulse time delay under different laser wavelengths, where the laser wavelength becomes shorter from the bottom to the top. The pulse time delay is an increasing trend when atmospheric visibility decreases. Moreover, the short wavelength leads to greater pulse time delay.

The pulse time delay of different laser wavelengths at various transmission distances is shown in Figure 7(a), where the atmospheric visibility is set as 1 km. The pulse time delay grows incrementally over the transmission distance under different light wavelengths.

Table 2 shows the pulse time delay of different laser wavelengths, where transmission distance is 300 m. This illustrates that the pulse time delay gradually increases when using short-wavelength lasers as the carrier. Consequently, longer wavelength is conducive to reducing the pulse time delay and the mutual interference when transmitting signals over a short distance in sand-dust weather conditions. The influence of atmospheric visibility on pulse time delay is described in Figure 7(b), where the transmission distance is set as 1 km. It is evident from the plot that the decline of pulse time delay follows a negative exponential trend relative to the atmospheric visibility. Furthermore, the pulse time delay tends to be a wavelength-dependent constant when the atmospheric visibility is greater than 3.5 km.

Figure 8(a) demonstrates the curves of pulse time delay versus the transmission distance at different scattering albedos, where the scattering coefficient is set as 7×10^{-4} . It is evident from the plot that the pulse time delay shows an exponential growth with increasing transmission distance. Table 3 shows the pulse time delay with the transmission distances, where $\omega = 0.6$. Moreover, the pulse time delay increases with increasing scattering albedo. As a result, the multipath effect caused by scattering is the main factor behind the pulse time delay when the scattering effect is stronger than the absorption effect. Figure 8(b) shows the influence of the scattering coefficient on pulse time delay when $\omega = 0.7$. It is evident from the figure that larger scattering coefficients result in longer pulse time delay. The reason for this phenomenon is that the larger scattering coefficient indicates higher sand-dust particle concentration in the atmosphere. Therefore, the probability of scattering is increased and leads to more serious multipath effect.

Figure 9 illustrates the relationship between pulse time delay and the asymmetry factor at different transmission distances when $\lambda = 10.6 \mu\text{m}$, $V = 1 \text{ km}$, and $C_s = 7 \times 10^{-4}$. As depicted in the plot, the pulse time delay decreases in a negative exponential trend with an

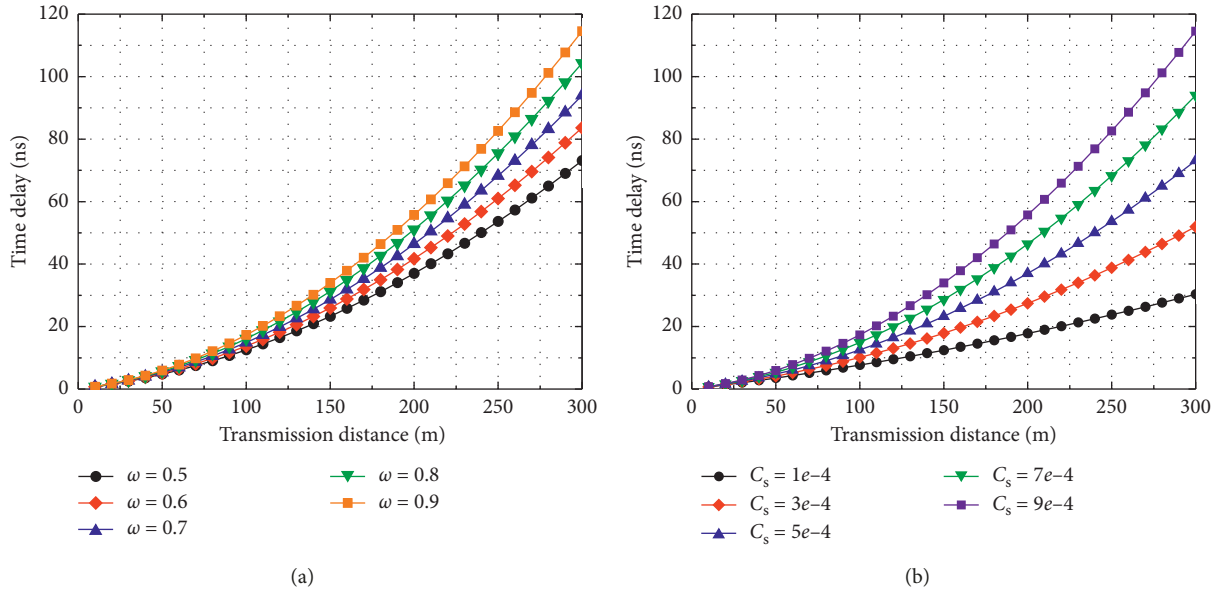


FIGURE 8: Pulse time delay as a function of transmission distance under (a) different scattering albedos and (b) different scattering coefficients.

TABLE 3: Pulse time delay at different transmission distances ($\omega = 0.6$).

Transmission distances (m)	Pulse time delay (ns)
50	5.1
100	13.7
150	25.9
200	41.7
250	60.9
300	83.6

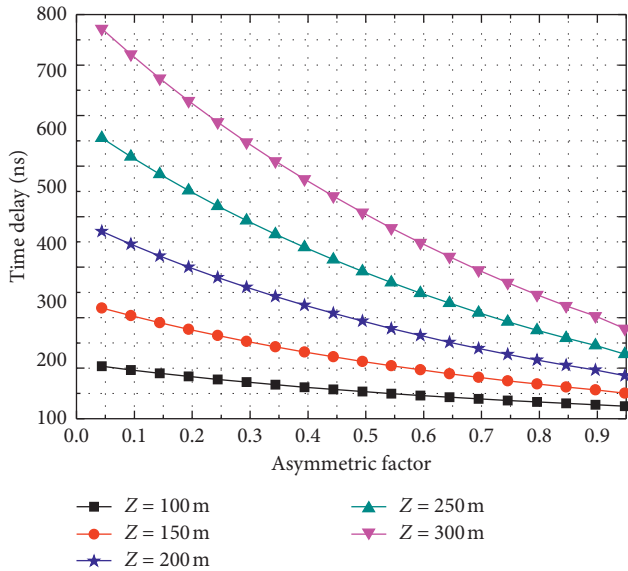


FIGURE 9: Pulse time delay as a function of the asymmetry factor.

increasing asymmetry factor. This is because forward scattering is predominant when the asymmetry factor gets close to 1.

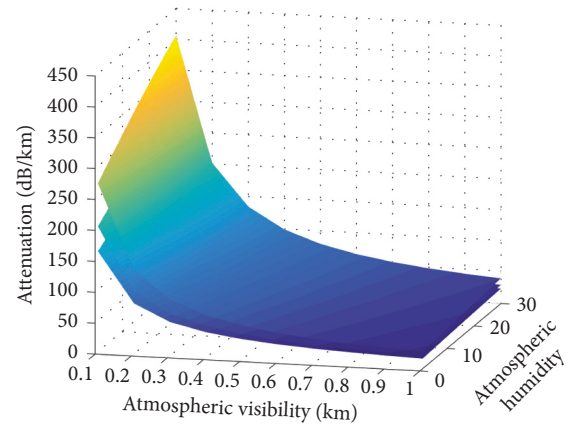


FIGURE 10: Laser signal attenuation as a function of atmospheric visibility and humidity under different laser wavelengths.

3.3. *Light Attenuation.* The light signal attenuation characteristics under sand-dust weather conditions are shown in Figures 10–12 based on the result of equation (43).

Figure 10 depicts laser signal attenuation as a function of atmospheric visibility and humidity under three different laser wavelengths, where the laser wavelength becomes shorter from the bottom to the top. It is evident from the figure that the signal attenuation is inversely proportional to atmospheric visibility and directly proportional to atmospheric humidity. This phenomenon is particularly evident in the short laser wavelength scenario.

Figure 11(a) shows signal attenuation versus atmospheric visibility with different laser wavelengths in linear-log coordinates, where the atmospheric humidity is set to 10%. It is evident from the figure that the attenuation follows a negative exponential decay trend with increasing atmospheric visibility. The attenuation eventually tends to be a constant when the atmospheric visibility increases to 5 km.

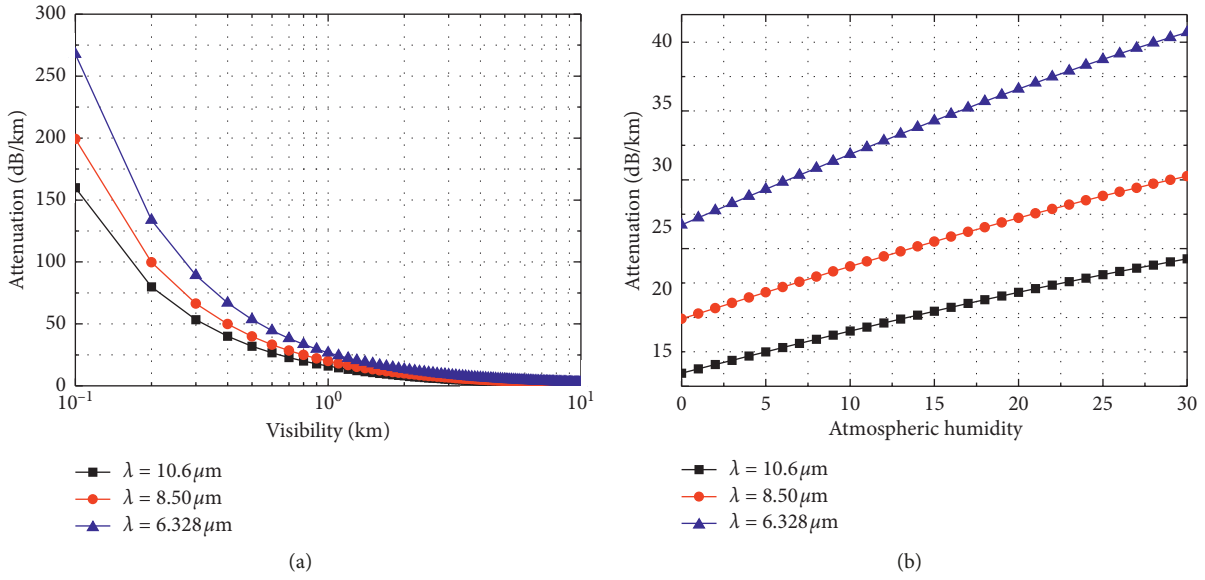


FIGURE 11: Laser attenuation of different laser wavelengths in (a) different atmospheric visibilities and (b) different atmospheric humidities.

TABLE 4: Attenuation of different laser wavelengths.

Laser wavelength (μm)	Attenuation (dB/km)		
	Atmospheric humidity (5%)	Atmospheric humidity (15%)	Atmospheric humidity (25%)
10.6	17.50	20.45	23.10
8.5	21.83	25.51	28.82
6.328	29.32	34.29	38.75

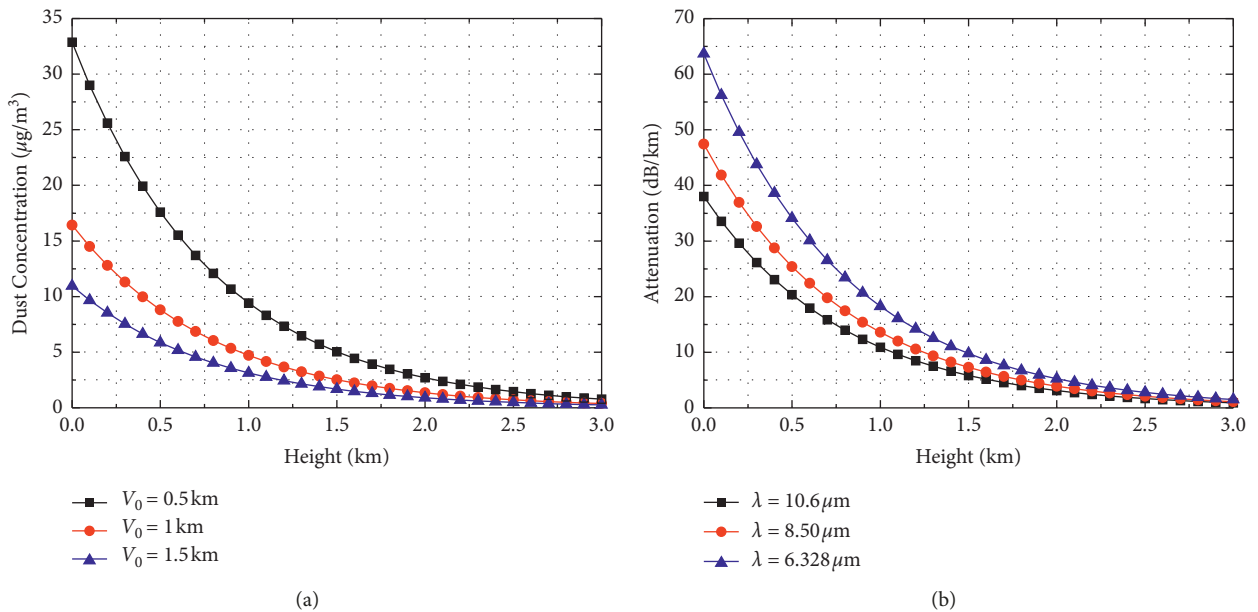


FIGURE 12: Sand-dust concentration and signal attenuation as a function of antenna transmission height under (a) different atmospheric visibilities and (b) different laser wavelengths.

Furthermore, it is clear that the attenuation decreases with increasing laser wavelength. Figure 11(b) illustrates signal attenuation versus atmospheric humidity under different laser wavelengths. The attenuation increases with increasing atmospheric humidity.

Table 4 shows the signal attenuation of different laser wavelengths, where the atmospheric humidity is 5%, 15%, and 25%, respectively. This indicates that the signal attenuation decreases with increasing laser wavelength. As a result, we can conclude that longer laser wavelengths can

help reduce signal attenuation when operating a laser communication system in sand-dust weather conditions.

Figure 12(a) demonstrates the relationship between sand-dust concentration and antenna transmission height under different levels of atmospheric visibility. It can be concluded from the figure that the sand-dust concentration shows a negative exponential decay trend to the antenna transmission height. Particularly, when the antenna transmission height increases beyond 2.5 km, the atmospheric sand-dust concentration reduces below $2.8 \mu\text{g}/\text{m}^3$ and gradually tends to be a constant. Figure 12(b) shows the influence of the antenna transmission height on signal attenuation with different laser wavelengths. It can be observed from the figure that the attenuation decreases with increasing antenna transmission height. Furthermore, it tends to be a constant value when the antenna transmission height exceeds 2.5 km. This is because the increased height leads to smaller atmospheric sand-dust concentration. Consequently, the effect of multiple scattering becomes less, which results in less attenuation.

4. Conclusion

We analysed the influential factors relevant to laser signal transmission in sand-dust weather conditions by utilizing the radiation propagation method and the small-angle approximation method. Simulation results were presented to evaluate the performance of laser signals transmitting through a sand-dust channel with scattering and absorption effects. Results indicate that sand-dust weather conditions cause significant light attenuation and pulse time delay. However, the results also indicate that longer laser wavelengths could potentially be utilized to improve the communication reliability of FSO systems in sand-dust weather conditions.

Data Availability

The data that support the findings of this study are available from the corresponding author upon reasonable request.

Conflicts of Interest

The authors declare that they have no conflicts of interest.

Acknowledgments

This work was supported in part by the NSFC Program (61875080, 61465007, and 61861026) and the Foundation of Gansu Education Department (2017A-011).

References

- [1] N. Kumar and H. Sohal, "Impact of various weather condition on the performance of free space optical communication system," *Journal of Optical Communications*, vol. 35, no. 1, pp. 45–49, 2014.
- [2] Z. Ghassemlooy, J. Perez, and E. Leitgeb, "On the performance of FSO communications links under sand-dust storm conditions," in *Proceedings of the IEEE International Conference on Telecommunications*, pp. 53–58, Zagreb, Croatia, July 2013.
- [3] M. Ijaz, Z. Ghassemlooy, J. Perez, V. Brazda, and O. Fiser, "Enhancing the atmospheric visibility and fog attenuation using a controlled FSO channel," *IEEE Photonics Technology Letters*, vol. 25, no. 13, pp. 1262–1265, 2013.
- [4] M. A. Esmail, H. Fathallah, and M.-S. Alouini, "Outdoor FSO communications under fog: attenuation modeling and performance evaluation," *IEEE Photonics Journal*, vol. 8, no. 4, pp. 1–22, 2016.
- [5] M. Singh, "Performance analysis of WDM-FSO system under adverse weather conditions," *Photonic Network Communications*, vol. 36, no. 4, pp. 1–10, 2018.
- [6] H. C. V. D. Hulst and V. Twersky, *Light Scattering by Small Particles*, Dover Publications, Mineola, NY, USA, 1981.
- [7] I. I. Kim, B. McArthur, and E. Korevaar, "Comparison of laser beam propagation at 785 nm and 1550 nm in fog and haze for optical wireless communications," in *Proceedings of the SPIE Optical Wireless Communications III*, vol. 4214, pp. 26–37, Boston, MA, USA, February 2001.
- [8] L. K. Harada and D. H. Leslie, "Atmospheric transmission analysis for airborne laser application," in *Proceedings of the SPIE Laser Beam Propagation and Control*, vol. 2120, pp. 56–73, Los Angeles, CA, USA, June 1994.
- [9] M. R. Islam, Z. E. Omer Elshaikh, O. O. Khalifa, A. Z. Alam, S. Khan, and A. W. Naji, "Prediction of signal attenuation due to duststorms using MIE scattering," *IJUM Engineering Journal*, vol. 11, no. 1, pp. 71–87, 2010.
- [10] H. Q. Wang, Y. G. Wang, M. H. Cao, and X. Z. Ke, "Influence of atmospheric visibility on laser pulse delay and broadening in sand and dust weather," *Acta Optica Sinica*, vol. 35, no. 7, Article ID 0701002, 2015.
- [11] D. W. Mackowski, "Discrete dipole moment method for calculation of the T matrix for nonspherical particles," *Journal of the Optical Society of America A*, vol. 19, no. 5, pp. 881–893, 2002.
- [12] S. Hu, T. Gao, H. Li et al., "Light scattering computation model for nonspherical aerosol particles based on multi-resolution time-domain scheme: model development and validation," *Optics Express*, vol. 25, no. 2, pp. 1463–1486, 2017.
- [13] P. González-Rodríguez and A. D. Kim, "Light propagation in tissues with forward-peaked and large-angle scattering," *Applied Optics*, vol. 47, no. 14, pp. 2599–2609, 2008.
- [14] S. Nguyen-Kuok, "Erratum to: classical theory of the particle scattering," in *Theory of Low-Temperature Plasma Physics*, Springer International Publishing, Berlin, Germany, 2017.
- [15] N. Pfeiffer and G. H. Chapman, "Successive order, multiple scattering of two-term Henyey-Greenstein phase functions," *Optics Express*, vol. 16, no. 18, pp. 13637–13642, 2008.
- [16] S. Shah, S. Mughal, and S. Memon, "Theoretical and empirical based extinction coefficients for fog attenuation in terms of visibility at 850 nm," in *Proceedings of the IEEE International Conference on Emerging Technologies*, pp. 1–4, IEEE, Peshawar, Pakistan, December 2015.
- [17] Y. M. Zhou, Q. Z. Liu, X. H. Zhang, and J. Sun, "An efficient method for simulating time-domain broadening of laser pulse propagating underwater," *Chinese Journal of Lasers*, vol. 36, no. 1, pp. 143–147, 2009.
- [18] Y. Yu, W. Huiqin, H. Qiu, P. Qingbin, and C. Minghua, "The air attenuation of laser transmission in sand-dust weather," in *Proceedings of the 16th International Conference on Optical Communications and Networks*, pp. 1–3, IEEE, Wuzhen, China, August 2017.
- [19] Q. S. Dong, "Physical characteristics of the sand-dust and sand-dust in different deserts of China," *Chinese Journal of Radio Science*, vol. 12, no. 1, pp. 15–25, 1997.

- [20] R. D. Smirnov, A. Y. Pigarov, S. I. Krasheninnikov, M. Rosenberg, and D. A. Mendis, "Simulation of sand-dust statistical characteristics in tokamaks," *Contributions to Plasma Physics*, vol. 48, no. 1-3, pp. 290-294, 2008.
- [21] H. Li and X. Sang, "SNR and transmission error rate for remote laser communication system in real atmosphere channel," *Sensors and Actuators A: Physical*, vol. 258, pp. 156-162, 2017.
- [22] A. Ahmed, A. Ali, and M. Alhaider, "Airborne dust size analysis for tropospheric propagation of millimetric waves into dust storms," *IEEE Transactions on Geoscience and Remote Sensing*, vol. GE-25, no. 5, pp. 593-599, 1987.
- [23] A. H. Sihvola and J. A. Kong, "Effective permittivity of dielectric mixtures," *IEEE Transactions on Geoscience and Remote Sensing*, vol. 26, no. 4, pp. 420-429, 1988.
- [24] Z. Wang, Z. D. Fang, H. D. Ting, H. U. Tao, and W. L. Wen, "Calculation and simulation of sand and dust attenuation in microwave propagation," *High Power Laser and Particle Beams*, vol. 17, no. 8, pp. 1259-1262, 2005.
- [25] W. J. Ellison, "Permittivity of pure water, at standard atmospheric pressure, over the frequency range 0-25 THz and the temperature range 0-100°C," *Journal of Physical and Chemical Reference Data*, vol. 36, no. 1, pp. 1-18, 2007.
- [26] E. A. A. Elsheikh, M. R. Islam, M. H. Habaebi, A. F. Ismail, and A. Zyoud, "Dust storm attenuation modeling based on measurements in Sudan," *IEEE Transactions on Antennas and Propagation*, vol. 65, no. 8, pp. 4200-4208, 2017.



Hindawi

Submit your manuscripts at
www.hindawi.com

